

Measurement of charge symmetry breaking by the comparison of $\pi^+ d \rightarrow pp \eta$ with $\pi^- d \rightarrow nn \eta$

W. B. Tippens,¹ V. Abaev,² M. Batinić,^{3,*} V. Bekrenev,² W. J. Briscoe,⁴ R. E. Chrien,⁵ M. Clajus,¹ D. Isenhower,⁶ N. Kozlenko,² S. Kruglov,² M. J. Leitch,⁷ A. Marušić,³ T. Moriwaki,⁶ T. Morrison,⁴ B. M. K. Nefkens,¹ J. C. Peng,⁷ P. H. Pile,⁵ J. W. Price,¹ D. Rigsby,⁶ M. E. Sadler,⁶ R. Sawafta,⁵ I. Šlaus,³ H. Seyfarth,⁸ A. Starostin,^{1,2} I. Supek,³ R. J. Sutter,⁵ A. Švarc,³ and D. B. White¹

¹University of California, Los Angeles, Los Angeles, California 90095-1547

²Petersburg Nuclear Physics Institute, Gatchina, Leningrad District, 188350, Russia

³Rudjer Bosković Institute, Zagreb 10000, Croatia

⁴George Washington University, Washington, D.C. 20052

⁵Brookhaven National Laboratory, Upton, New York 11973

⁶Abilene Christian University, Abilene, Texas 79699

⁷Los Alamos National Laboratory, Los Alamos, New Mexico 87545

⁸Forschungszentrum, Jülich D-52425, Jülich, Germany

(Received 16 June 2000; published 6 February 2001)

We report a measurement of charge symmetry breaking in the $NN\eta$ system. We have measured the ratio of the differential cross sections of the charge-symmetric reactions $\pi^+ d \rightarrow pp \eta$ and $\pi^- d \rightarrow nn \eta$ in the energy region of the η threshold. Our result is $R \equiv d\sigma(\pi^+ d \rightarrow pp \eta)/d\sigma(\pi^- d \rightarrow nn \eta) = 0.938 \pm 0.009$ after a phase-space correction is made for the difference in the threshold energies of the two reactions. The deviation of R from unity is an indication of charge symmetry breaking, which is mostly due to π^0 - η mixing. A theoretical model for η production which includes π^0 - η mixing was used to fit the data and yields a mixing angle of $(1.5 \pm 0.4)^\circ$. Our result is consistent with the mixing angle determined in particle decay and isospin-forbidden processes as well as predictions by several theoretical analyses which yield $\approx 1^\circ$ and another which yields $\approx 2^\circ$.

DOI: 10.1103/PhysRevD.63.052001

PACS number(s): 14.40.Aq, 24.80.+y, 13.75.-n

I. INTRODUCTION

Charge symmetry (CS) is the invariance of the strong interaction under the interchange of the up and down quarks [1]. The charge symmetry operator P_{cs} changes d quarks into u quarks and vice versa:

$$P_{cs}|d\rangle = |u\rangle, \quad P_{cs}|u\rangle = -|d\rangle. \quad (1)$$

The Lagrangian of QCD can be separated into two parts: $\mathcal{L} = \mathcal{L}_{fi} + \mathcal{L}_m$. The first term \mathcal{L}_{fi} is flavor independent because it has only quark and gluon fields. The second term \mathcal{L}_m depends on the quark fields and the current quark masses which cause the violation of flavor symmetry in QCD:

$$\mathcal{L}_m = -m_d d\bar{d} - m_u u\bar{u} - \dots \quad (2)$$

Flavor independence is the assumption that the strong interaction is equal for all quark flavors when quarks are massless. Charge symmetry is the manifestation of this with reference to the u and d quarks. Since quarks have an electric charge and magnetic moment, QED breaks flavor independence. The charge symmetry breaking (CSB) resulting from the ≈ 3 MeV mass difference of the u and d quarks is referred to as intrinsic CSB.

One way intrinsic CSB can manifest itself is through meson mixing. A well known example of this in nuclear systems is ρ^0 - ω mixing as seen, for instance, in the ratio of the reactions $\pi^+ d \rightarrow \pi^+ \pi^- pp$ and $\pi^- d \rightarrow \pi^+ \pi^- nn$ in the re-

gion of the ω threshold [1–3], see Fig. 1. The matrix element for ρ^0 - ω mixing of the isospin eigenstate in the Hamiltonian representation is proportional to the u - d quark mass difference:

$$\langle \tilde{\rho}^0 | H_m | \tilde{\omega} \rangle = \left\langle \frac{1}{\sqrt{2}}(u\bar{u} - d\bar{d}) \left| m_d d\bar{d} + m_u u\bar{u} \right| \frac{1}{\sqrt{2}}(u\bar{u} + d\bar{d}) \right\rangle \quad (3a)$$

$$= \frac{1}{2}(m_u - m_d), \quad (3b)$$

where the tilde over a bra or ket vector represents the isospin eigenstates. In an analogous fashion, the pseudoscalar π^0 - η mixing is also found to be proportional to the u - d mass difference alone, due to the negligibly small $s\bar{s}$ contribution to the π^0 meson:

$$\langle \tilde{\pi}^0 | H_m | \tilde{\eta} \rangle = \left\langle \frac{1}{\sqrt{2}}(u\bar{u} - d\bar{d}) \left| m_d d\bar{d} + m_u u\bar{u} + m_s s\bar{s} \right| \frac{1}{\sqrt{3}}(u\bar{u} + d\bar{d} - s\bar{s}) \right\rangle \quad (4a)$$

$$= \frac{1}{\sqrt{6}}(m_u - m_d). \quad (4b)$$

We assume here that the η is a pure $q\bar{q}$ state with an ignorable small gluon component. We have used $\theta_V = 35.3^\circ$ for

*Deceased.

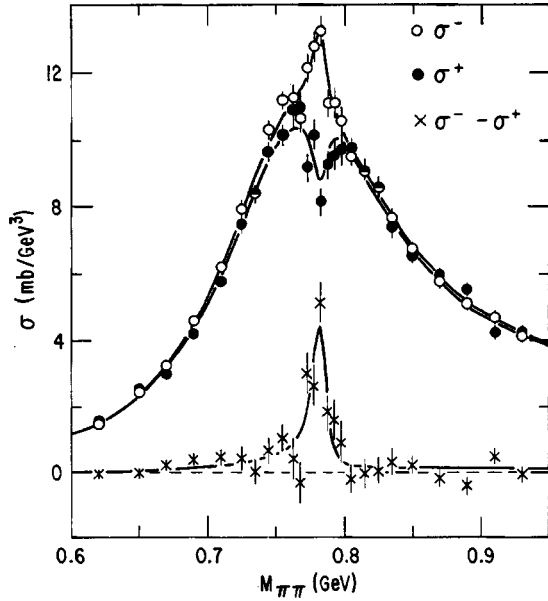


FIG. 1. Example of ρ^0 - ω mixing obtained in a measurement of $\pi^- d \rightarrow \pi^+ \pi^- nn$ (\circ) and $\pi^+ d \rightarrow \pi^+ \pi^- pp$ (\bullet) from Ref. [2].

the vector octet-singlet mixing in the isospin eigenstate $\tilde{\omega}$ and $\theta_p = -19.5^\circ$ for the pseudoscalar octet-singlet mixing in $\tilde{\eta}$. These values have good experimental and theoretical justification [4]. The physical π^0 and η mesons are represented as mixtures of the meson isospin eigenstates described by a π^0 - η mixing angle $\theta_{\pi\eta}$:

$$|\pi^0\rangle = \cos \theta_{\pi\eta} |\tilde{\pi}^0\rangle + \sin \theta_{\pi\eta} |\tilde{\eta}\rangle, \quad (5a)$$

$$|\eta\rangle = -\sin \theta_{\pi\eta} |\tilde{\pi}^0\rangle + \cos \theta_{\pi\eta} |\tilde{\eta}\rangle. \quad (5b)$$

This is the mixing angle which we wish to determine from the ratio of the differential cross sections for $\pi^\pm d \rightarrow NN\eta$.

This π^0 - η mixing has been clearly observed in selected decays, specifically in the ratio of the CSB to CS-conserved decay rates: $R_1 = \Gamma(\eta' \rightarrow 3\pi^0)/\Gamma(\eta' \rightarrow 2\pi^0\eta)$ and $R_2 = \Gamma(\psi' \rightarrow \psi\pi^0)/\Gamma(\psi' \rightarrow \psi\eta)$. It also contributes to the difference in the nn and pp scattering lengths, the magnitude of the analyzing power in the $n\eta$ interaction, and the Nolen-Schiffer anomaly [1]. Detailed model calculations indicate that these phenomena are dominated by ρ^0 - ω mixing, and the uncertainties in the calculations make the drawing of conclusions on π^0 - η mixing difficult.

The difference between the ρ^0 and ω masses (≈ 12 MeV) is much smaller than the difference between the π^0 and η masses (≈ 412 MeV). Also, the π^0 and the η widths (7.8 ± 0.6 eV and 1.20 ± 0.11 keV, respectively) are much narrower than the ρ^0 (151.2 ± 1.2 MeV). It could be that the large mass difference between the π^0 and the η suppresses mixing effects in low energy processes where the η is only a virtual particle that is far off-mass-shell.

This experiment was designed to study on-shell π^0 - η mixing by measuring the ratio

$$R = d\sigma(\pi^+ d \rightarrow pp\eta) / d\sigma(\pi^- d \rightarrow nn\eta) \quad (6)$$

in the region of the η threshold. Charge symmetry requires that this ratio be equal to unity at all incident pion energies and for all final state kinematics after an adjustment has been made for Coulomb interactions and the n - p mass difference. It is possible that π^0 - η mixing could be strongly enhanced by the N^* resonance $S_{11}(1535)$, which decays largely via the ηN (30–55 %) and $\pi^0 N$ (35–50 %) channels.

Flavor symmetry of u , d , and s quarks is apparent in SU(3) symmetry, which is observed in baryon and meson spectroscopy, despite the sizeable mass difference between the s and u or d quarks. CSB provides us with a means of evaluating the mass difference of the u and d quarks. There is much evidence for CSB but most of it is static (the difference between particle masses) or for a particular momentum transfer, such as the difference in isospin related decay rates. The reactions $\pi^\pm d \rightarrow NN\eta$ offer the possibility to investigate the dependence of CSB on total energy and momentum transfer. This is of interest because QCD implies that CSB should be dependent on energy and the nuclear environment.

II. THEORETICAL MODEL FOR η PRODUCTION WITH π^0 - η MIXING

In order to extract the magnitude of π^0 - η mixing using the reactions $\pi^\pm d \rightarrow NN\eta$, a theoretical model for this process is needed that includes the following:

The effect of the n - p mass difference and Coulomb energy. The n - p mass difference causes an energy difference of 2.6 MeV between the reaction thresholds. The Coulomb energy between the charged pions and the deuteron reduces this effect by ≈ 0.8 MeV [5] for a total effective energy difference $E_{th}(\pi^- d) - E_{th}(\pi^+ d) \approx 1.8$ MeV. This corresponds to a relative beam momentum threshold difference of ≈ 2.6 MeV/ c , which affects the phase space for each reaction differently.

The mass splitting of the $S_{11}(1535)$ doublet. The u - d mass difference of ≈ 3.4 MeV gives a mass splitting between the S_{11}^+ and the S_{11}^0 of 3.8 MeV. The Coulomb correction to the masses is estimated to be $E_c(udd) - E_c(uud) \approx -2$ MeV. This gives an overall mass difference of ≈ 1.8 MeV.

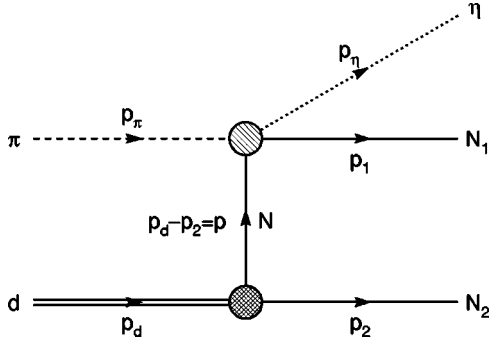
The difference in the widths of the $S_{11}(1535)$ doublet. We are not aware of an estimate for this.

The difference in the meson-nucleon coupling constants $nn\eta$ and $pp\eta$. It is argued in Ref. [6] that the CSB effects are about -1.1% for $nn\eta$ and $+1.1\%$ for $pp\eta$.

Differences in the final state interactions between the nucleons.

A phenomenological model of the $\pi^\pm d \rightarrow NN\eta$ process has been developed by members of our collaboration [7] based on the coupled channel πn - ηn amplitudes from Ref. [8]. A fully relativistic calculation of the $\pi d \rightarrow NN\eta$ process is performed, based on the dominant diagram shown in Fig. 2.¹ The invariant matrix element [9] describing this process is

¹It should be noted that some of the next-order diagrams are effectively included in the model since experimental data were used to determine the $\pi N \rightarrow \eta N$ T -matrices.

FIG. 2. The dominant diagram for the $\pi d \rightarrow NN\eta$ process.

$$\mathcal{M}_{\lambda_d, \lambda_1 \lambda_2} = \frac{1}{2} \left\{ \bar{u}_{\lambda_1}(\mathbf{p}_1) [A + \not{p}_\eta B] \frac{\not{p}_d - \not{p}_2 + m}{(p_d - p_2)^2 - m^2} \right. \\ \left. \times [\epsilon_{\lambda_d} G_a + (p_2 \cdot \epsilon_{\lambda_d}) G_b] v_{\lambda_2}(\mathbf{p}_2) - (1 \leftrightarrow 2) \right\}. \quad (7)$$

We use the Bjorken-Drell convention: $p_\pi, p_d, p_\eta, p_1, p_2$ are the four-momenta and $\lambda_d, \lambda_1, \lambda_2$ are the helicities, with the subscripts given in Fig. 2. u and v are nucleon Dirac spinors, ϵ_{λ_d} is the deuteron rotation parameter, and m is the exchanged-nucleon mass. The $\pi N - \eta N$ vertex is described by the invariant functions A and B (functions of the πN center of mass energy W and angle θ) which have been expanded using $\pi N \rightarrow \eta N$ partial wave T -matrices generated from the coupled channel partial wave analysis of Ref. [8]. The $n-p-d$ vertex is described by the invariant functions G_a and G_b which are fitted to modern electron scattering data of the deuteron [10].

The differential cross section is expressed as

$$\frac{d^5 \sigma}{dp_\eta d\Omega_\eta d\Omega_1} = |M_{fi}^{tot}|^2 \frac{\Phi}{\Psi} J_{fsi}, \quad (8a)$$

$$\text{with } \Phi = \frac{p_\eta^2 p_1^2 m^2}{64 \pi^5 W_\eta (p_1 W_2 - W_1 \hat{\mathbf{p}}_1 \cdot \mathbf{p}_2)}, \quad (8b)$$

$$\text{and } \Psi = \sqrt{(p_\pi \cdot p_d)^2 - m_\pi^2 m_d^2}. \quad (8c)$$

Φ is the phase space for the reaction, Ψ is the flux, and J_{fsi} is the final state interaction (FSI) for which we have used a standard Jost 1S_0 function which depends on the relative nucleon-nucleon momentum. The W_i represent the c.m. energies for the appropriate particles. Coulomb effects are included for the pp final state. We used -18.5 fm and -17.6 fm for the nn and pp 1S_0 scattering lengths, respectively, and 2.86 fm for both effective ranges [1,11]. The FSI between the η and the nucleon was neglected. No initial state interactions were included.

The $\pi^0 - \eta$ mixing was incorporated in the functions A and B via the $\pi N \rightarrow \eta N$ T -matrices. This is done by expressing the matrix elements for the transition operator of the physical particles for the two free production reactions using Eq. (5b):

$$T(\pi^- p \rightarrow \eta n) \equiv \langle \pi^- p | T | \eta n \rangle = \cos \theta_{\pi\eta} T_{\tilde{\eta}}^- - \sin \theta_{\pi\eta} T_{\tilde{\pi}^0}^-, \quad (9)$$

$$T(\pi^+ n \rightarrow \eta p) \equiv \langle \pi^+ n | T | \eta p \rangle = -\cos \theta_{\pi\eta} T_{\tilde{\eta}}^- - \sin \theta_{\pi\eta} T_{\tilde{\pi}^0}^-, \quad (10)$$

where $T_{\tilde{\pi}^0}^-$ and $T_{\tilde{\eta}}^-$ are defined as

$$T_{\tilde{\pi}^0}^- = \langle \pi^- p | T | \tilde{\pi}^0 n \rangle = \langle \pi^+ n | T | \tilde{\pi}^0 p \rangle, \quad (11)$$

$$T_{\tilde{\eta}}^- = \langle \pi^- p | T | \tilde{\eta} n \rangle = -\langle \pi^+ n | T | \tilde{\eta} p \rangle. \quad (12)$$

$T(\pi^+ n \rightarrow \eta p)$ then can be obtained from the T -matrices for $\pi^- p \rightarrow \eta n$ and $\pi^- p \rightarrow \pi^0 n$:

$$T(\pi^+ n \rightarrow \eta p) = -T(\pi^- p \rightarrow \eta n) \\ - 2 \sin \theta_{\pi\eta} T(\pi^- p \rightarrow \pi^0 n). \quad (13)$$

If we assume that all CSB in $\pi d \rightarrow \eta NN$ processes is associated with η production, we can write the ratio of the cross sections as

$$R \approx 1 + 4 \tan \theta_{\pi\eta} \text{Re} \left(\frac{T_{\tilde{\pi}^0}^-}{T_{\tilde{\eta}}^-} \right). \quad (14)$$

Thus, the deviation of R from unity is very sensitive to a non-zero value for the mixing angle.

The result of the coupled channel partial wave analysis [8] yields $\pi^- p \rightarrow \eta n$ partial wave T -matrices that can be used for the $\pi^- d \rightarrow \eta nn$ calculations. We can include the $\pi^0 - \eta$ mixing to first order in the mixing angle $\theta_{\pi\eta}$ to obtain the $\pi^+ n \rightarrow \eta p$ T -matrices to be used for the $\pi^+ d \rightarrow \eta pp$ calculations:

$$T(\pi^+ n \rightarrow \eta p) = \frac{K_{\pi^+ n}}{K_{\pi^- p}} \left[-T^{PWA}(\pi^- p \rightarrow \eta n) \frac{K_{\eta p}}{K_{\eta n}} \right. \\ \left. - 2 \sin \theta_{\pi^0 \eta} T^{PWA}(\pi^- p \rightarrow \pi^0 n) \frac{K_{\eta p}}{K_{\pi^0 n}} \right]. \quad (15)$$

The kinematical factors K_{ij} ensure good threshold behavior. For $T^{PWA}(\pi^- p \rightarrow \pi^0 n)$ we have used the SAID SM95 solution [12], and our own coupled channel partial wave analysis [8] for $T^{PWA}(\pi^- p \rightarrow \eta n)$.

In the above relations, we have ignored some kinematic factors such as CSB differences in the $S_{11}^+ - S_{11}^0$ doublet. These effects are of the order $m_{S_{11}^+} - m_{S_{11}^0} \approx -0.7$ MeV per degree $\theta_{\pi\eta}$. For example, in the S_{11} partial wave we have $m_{S_{11}^+} - m_{S_{11}^0} = -0.2$ MeV for $\theta_{\pi\eta} = 0$, while $m_{S_{11}^+} - m_{S_{11}^0} = -1.6$ MeV for $\theta_{\pi\eta} = 2^\circ$.

In terms of the invariant matrix element, the differential cross section for the complete experiment can be written as

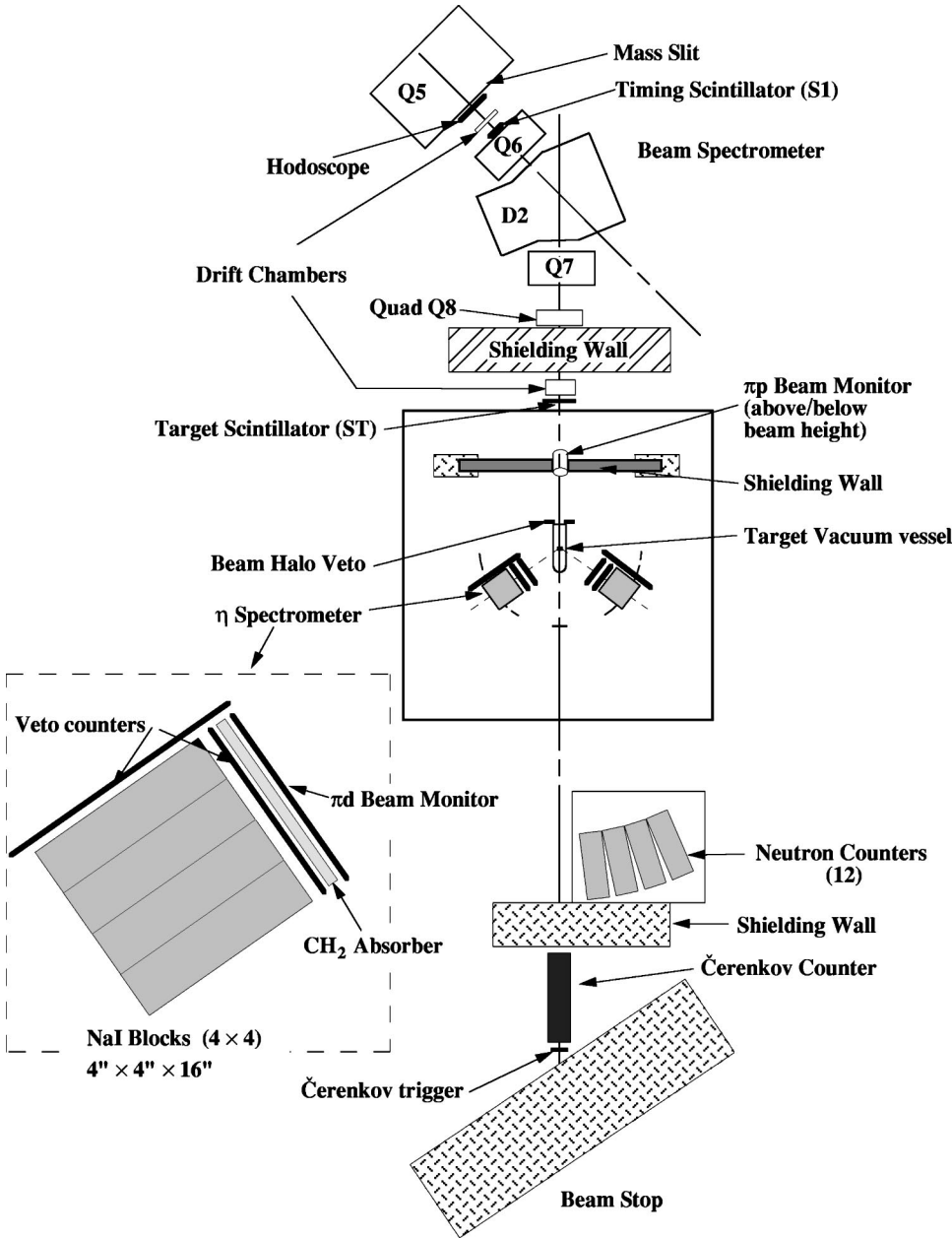


FIG. 3. Floor layout showing the C8 beamline after the separators and the experimental setup.

$$\frac{d^5\sigma}{dp_\eta d\Omega_\eta d\Omega_1} = \frac{|M_{\lambda_d \lambda_1 \lambda_2}|^2}{\sqrt{(p_\pi \cdot p_d)^2 - m_\pi^2 m_d^2}} \times \frac{p_\eta^2 p_1^2 m^2}{64\pi^5 W_\eta (p_1 W_2 - W_1 \hat{\mathbf{p}}_1 \cdot \mathbf{p}_2)} J_{fsi}. \quad (16)$$

In order to compare the data to the model, it was easier to calculate experimental yields directly by calculating the “differential acceptance,” $A(p_\eta, \theta_\eta)$, which gives the probability of this experiment detecting η ’s emitted with lab momentum p_η at the lab angle θ_η , uniformly distributed over ϕ_η . The total cross section and acceptance were determined by integration over the η angle and momentum variables:

$$Y_{exp} \propto E \int dp_\eta \int d\Omega_\eta A(p_\eta, \Omega_\eta) \int d\Omega_1 \frac{d^5\sigma}{dp_\eta d\Omega_\eta d\Omega_1}, \quad (17)$$

where E is the overall detector efficiency. From these quantities, the actual yields in our detector are predicted by the model.

III. EXPERIMENTAL LAYOUT

The floor layout of the experiment is shown in Fig. 3. It includes the beamline downstream of the particle velocity separator, the liquid deuterium target, the spectrometer for detecting the photons from the η decay, and the beam stop. Not shown is the beamline upstream of the particle velocity separator consisting of the bending magnet, D1, which se-

lects the polarity and momentum of the channel, two pairs of focusing quadrupoles, Q1–Q4, and two $\vec{E} \times \vec{B}$ field separators. Further details of the detector as well as data taking and data analysis are given in the dissertation by Marušić [9].

A. C8 beamline

The experiment was conducted in the C8 beamline of the AGS at Brookhaven National Laboratory. This beamline normally delivers a separated, momentum-recombined beam of pions, kaons, or antiprotons up to a maximum momentum of ≈ 750 MeV/ c . The “mass slit” in Fig. 3 consists of a pair of tungsten jaws that are vertically adjustable and located at the vertical focus of the beamline located in the aperture of Q5 downstream of the two $\vec{E} \times \vec{B}$ field separators. The last three quadrupoles, Q6–Q8, and the wedge dipole magnet D2 provide the final control of the pion beams on target. They are also used as a momentum spectrometer to determine the individual momentum of the pions. The beam drift chambers provide the track information necessary to make the momentum measurement. They also give the individual pion x , y coordinates at the target which were used in the offline analysis to reduce background from the beam halo. A telescope, horizontal hodoscope was mounted immediately upstream of the first drift chamber to resolve multiple hit ambiguities arising from the high instantaneous rate in this region.

The beamline was originally designed to produce kaon beams with a large angular divergence and momentum dispersion for maximum flux. These features produce a beam of a very large cross-sectional area which is unacceptable for our purposes. Since the pion flux was much larger than needed, we obtained a smaller, less divergent beam with 1% momentum dispersion by reducing the momentum acceptance. This was accomplished by reversing the polarity of the first two quadrupoles of the beamline which determine the beamline acceptance. The beam size was reduced further by inserting a horizontal brass collimator just downstream of the mass slit. The brass collimator pieces were each 45.7 cm long and 1.27 cm wide. They formed a horizontal gap of 6.4 cm.

A 30 cm thick steel wall, which contained a lead collimator with a 11 cm wide by 10 cm high aperture, was located immediately downstream of Q8 and provided primary shielding of the experiment from beam-related background. This aperture was enlarged during phase II to 19×18 cm² to accommodate a larger beam. A second steel wall, 15 cm thick, shielded the spectrometer from beam scattering by the lead collimator and secondary particles. This wall was located 122 cm downstream of the primary wall and had a 30 cm square opening for the beam so as not to provide additional scattering. After passing through the target, the beam was absorbed in a concrete beam stop; another shield wall of concrete was located immediately upstream of a gas Čerenkov counter to shield the experiment from back-scattered particles from the stopped beam. The cylindrical gas Čerenkov counter was 25 cm in diameter and 128 cm long; it was used to measure the electron contamination of the beam. A $15.2 \times 15.2 \times 1.9$ cm³ scintillator was located behind the

counter to define the beam for monitoring the electron contamination.

A 3 mm thick lead foil was mounted in the upstream entrance to the “mass-slit” collimator to reduce the number of electrons in the beam. At 720 MeV/ c , this foil reduced the electron contamination from 50% to about 3%.

The beam trigger was formed by a coincidence between scintillator S1 ($6.0 \times 7.0 \times 0.64$ cm³), just upstream of the entrance to Q6, and ST ($5.0 \times 5.0 \times 0.64$ cm³), located 623 cm and 181 cm upstream of the target, respectively. Four scintillation veto paddles located 62 cm upstream of the target defined a 2.6×2.8 cm² rectangular aperture for the beam; all beam particles outside this aperture were rejected.

The relative pion flux was monitored by two scintillation counters ($14 \times 14 \times 1.0$ cm³) mounted 88 cm downstream from ST, one above and the other below the beam, such that each made an angle of 50° to the beam axis. These counters measured π - p elastic scattering from the hydrogen in the ST counter at the “symmetric” scattering angle ($\theta_\pi = \theta_p$) for our momentum range. This geometry allowed for the simultaneous detection of the pion and the proton in both counters either as pion-up and proton-down or vice versa. The ratio of pion-up to pion-down events provided a good beam alignment monitor. This reduced systematic errors due to differences in the π^+ and π^- beam positions. Particle identification was obtained using pulse height and time-of-flight (TOF) information.

We minimized the relative difference in momentum between the π^+ and π^- beams by carefully monitoring the ratio of the currents in the two bending magnets, D1 (not shown in Fig. 3) and D2. Since D2 was used as the momentum spectrometer, its current was kept constant and adjustments were made to the D1 current to maintain constant beam conditions; this insured that we had the same beam momentum at the target. The magnet currents for the beamline were established so as to remove hysteresis effects when reversing polarities. We found a systematic difference between the π^+ and π^- settings for D1 which would appear to correspond to a difference in momentum of about 10 MeV/ c . The difference, however, is attributed to the horizontal steering of the beam by the quadrupole Q4 (not shown in Fig. 3). Q4 is located between D1 and D2 and vertically focuses the beam at the mass slit. This steering was minimized by the heavy collimation of the beam which selected only the central portion of the beam. TOF measurements, described below, with K^\pm mesons confirmed that the different settings for D1 did not result in a difference in momentum for the π^\pm beams.

The absolute beam momentum was obtained by calibrating D2 using two different methods. One was TOF measurements using a kaon beam at various momenta over the range of the experiment. The other used TOF measurements of neutrons from the $\pi^- p \rightarrow \eta n$ reaction to determine the beam momentum relative to the known beam momentum for the η threshold at 684.7 MeV/ c . This required replacing the deuterium target with liquid hydrogen. The bank of neutron counters shown in Fig. 3 was used for this purpose.

B. The η spectrometer

The η meson was identified via the decay mode $\eta \rightarrow 2\gamma$. The two photons were detected by the η spectrometer made of two NaI calorimeters which were mounted on movable arms attached to a common pivot underneath the target. The length of the arms was also adjustable. Each calorimeter was a 4×4 array of crystals, each $10.2 \times 10.2 \times 40.6$ cm³ in size. Each crystal was housed in a 0.5 mm thick stainless steel canister with a 0.8 cm thick glass window for the coupling to an 8.9 cm diameter phototube. These calorimeters were the central part of the Los Alamos η spectrometer, which was built originally by Peng *et al.* in 1986 [13]. The spectrometer was used to measure the energy and position of the incident photons. Each arm was mounted on separate air pads so they could be moved independently.

In Fig. 3 one can see a blowup of one spectrometer arm. The elements of each arm, in order of traversal by the photon from the target, are the following: (a) three vertical, non-overlapping scintillation counters of dimension $13.3 \times 43.2 \times 0.6$ cm³ to provide an initial charged particle veto, (b) a 2.5 cm thick, borated polyethylene absorber mounted immediately behind the vertical vetoes to stop low energy protons and neutrons, (c) a second layer of horizontal, overlapping scintillation counters of dimension $15.2 \times 48.3 \times 0.6$ cm³ placed immediately in front of the NaI blocks for a charged particle veto, (d) the NaI crystals mounted in an open-faced aluminum box behind these counters, and (e) a plane of horizontally-mounted scintillation counters installed on the upstream side of the calorimeters to veto charged particles coming from beam scattering upstream of the target. These counters extended beyond the NaI blocks to cover their front faces and eliminate any dead spaces for the active veto system. The rates in these counters were very low as a result of the second steel wall which shielded the spectrometer.

The neutral event trigger was generated by the coincidence of a beam event and a spectrometer event. The beam event is the coincidence between the two beam counters S1 and ST in anti-coincidence with the four beam halo veto counters. A spectrometer event is the coincidence of the signals from the NaI counters in both spectrometer arms. We required that the energy deposited in each arm be greater than 150 MeV. The spectrometer veto counters were not part of the trigger.

Data were taken with two different triggering configurations of the spectrometer, referred to as phases I and II, see Sec. IV. This was done to study systematic errors in the spectrometer system. In phase I the spectrometer energy sum consisted of the inner four NaI counters of each arm. In phase II all of the crystals for each arm were summed to form the signal; but a lead collimator with a 30.5×30.5 cm² opening was placed in front of each NaI array, between the two sets of front vetoes, with the polyethylene absorber inside its aperture. This provided a well defined photon aperture for the triggering of the spectrometer which was larger than the inner four counters but smaller than the full area of the NaI array. The larger aperture increased the acceptance of each arm of the spectrometer by more than a factor of two.

All interactions in the spectrometer elements and target were simulated using the GEANT 3.21 software package from CERN [14]. This simulation was used to understand the calibration and backgrounds. The combined energy and angular resolution of the spectrometer as measured by the σ -width of the η invariant mass ranged from 3 to 6% depending on the beam momentum and opening angle setting. The variation in resolution was due to the coarse angular resolution of the spectrometer which is the combined result of the size of the crystals and the close proximity of the calorimeter counters to the target. The length of the spectrometer arms was chosen as a compromise between angular resolution and acceptance.

C. The liquid deuterium target

The target flask was a horizontal cylinder 2.6 cm long made of 0.13 mm thick mylar. It was 6.3 cm in diameter and had rounded endcaps. The maximum target length along the beam axis was 6.1 cm. The target length was kept small to minimize the degradation of resolution due to the uncertainty in the interaction vertex. The cylindrical wall was wrapped with 30 layers of superinsulation, and 20 layers were used on the spherical endcaps through which the beam passed. The latter was done to reduce background from beam interactions in the target flask. The vacuum chamber surrounding the target volume had the shape of an elongated clam shell that was 58.4 cm long, 15.2 cm wide, and 12.7 cm high. A 0.64 mm thick mylar window covered the aperture of the chamber which allowed laboratory angles for each spectrometer arm to be as large as $\approx 170^\circ$. The beam entered the vacuum chamber through a 10.2 cm diameter, 0.64 mm thick mylar window in the upstream face.

Any hydrogen in the liquid deuterium would make a direct, charge-asymmetric contribution. A chemical analysis of our liquid deuterium indicated 0.93% of HD and less than 0.015% of H₂ contamination for our phase I samples. The latter is the limit in sensitivity of the analysis and is consistent with zero. During phase II of the experiment, analytical grade deuterium gas was used. This provided a check on the 1% correction made to the ratio R for the hydrogen contamination in phase I.

IV. EXPERIMENTAL METHOD

The incident beam momentum was varied from 655 MeV/ c where the η yield is quite small up to 752 MeV/ c . The specific values of our π^+ and π^- beam momenta are enumerated in Tables III and IV discussed in Sec. VIII and Sec. IX.

The configuration of the η spectrometer was chosen to optimize the η yield. The distance of each NaI calorimeter to the deuterium target was set to 47.5 cm for most of the experiment. In phase I, one complete ratio measurement was made with the distance increased to 87.5 cm at 752 MeV/ c beam momentum to investigate $2\pi^0$ background under the η invariant mass peak. The angle of each arm, measured relative to the beam axis, was chosen to be the same. The angle was experimentally selected to maximize the η yield. The value of this angle for both sets of data varied from 75° for

the lowest beam momentum to 55° at the highest; corresponding to nominal opening angles of $150^\circ - 110^\circ$, respectively. In general, this procedure favored η production in the forward direction and the spectrometer arm angle to be placed near the maximum of the Jacobian. During phase I, we took 752 MeV/ c data at four different opening angles to investigate the dependence of the η production asymmetry on the opening angle.

In phase I, the spectrometer acceptance was restricted by the trigger to the central four NaI blocks; this configuration gives a high resolution for the η invariant mass because the energy leakage from the outer edges of the NaI arrays is small. In phase II we placed lead collimators, described in Sec. III B, in front of the NaI calorimeters and accepted signals from all of the crystals in the trigger. This gave a well defined angular acceptance which extended to the centers of the outer layer of NaI crystals, increasing our acceptance at the expense of a reduced invariant mass resolution.

Data with a liquid hydrogen target were taken at the end of the experiment (phase II) to compare with our Monte Carlo (MC) calculation of the π^-p reactions.

V. BEAM MOMENTUM DETERMINATION

The beam momentum calibration required the determination of the absolute beam momentum measured by the beam spectrometer as well as the relative beam momentum and phase space between the π^+ and π^- beams. Since our test of charge symmetry breaking involved a ratio of η production for π^+ and π^- beams, it was essential to maintain the same momentum for each beam polarity. Because the momentum dispersion was about 1%, we wanted to achieve a constant momentum to within a few MeV/ c .

The primary means of calibration used high precision direct TOF measurements of kaons and protons in the beam. K^+ and K^- mesons were used to determine any differences in the π^+ and π^- beam momenta. The protons provided our only calibration data for beam momenta below 700 MeV/ c . The technique used two counters in the flight path of the beam, one located at the position of ST and the other (not shown in Fig. 3) immediately in front of the Čerenkov counter. This provided a flight path of 637.9 ± 0.5 cm. The signals from these counters went to constant fraction discriminators which supplied stop signals to two independent time to digital converters (TDC)'s for each counter. These TDC's were calibrated periodically throughout the data taking period using an 80.000 MHz precision oscillator.

The TOF measurements were made in pairs with the rear TOF counter first located in its normal position, in front of the Čerenkov counter, and then moved forward to a position just behind the forward TOF counter. The beam TOF was determined by taking the difference of the statistical averages of the two beam TOF distributions for every pair of measurements. This technique gave a time resolution better than 35 ps at the highest momentum. Monitoring the mean and sigma values of the electron peak in the TOF distributions provided a real time check on systematic drifts. Absolute measurements were obtained with a precision of 2.5 MeV/ c . Energy loss corrections due to the material in the flight path includ-

ing the target assembly and air were made to the TOF measurements.

After the experiment, an independent calibration was done by measuring the neutron TOF from the reaction $\pi^-p \rightarrow \eta n$ with the liquid deuterium replaced by liquid hydrogen. This method was obviously restricted to π^- beam momenta above the η threshold. Two measurements were made at 725 and 749 MeV/ c . Four large plastic scintillation counters placed 387 cm downstream of the target were used to detect the neutrons with a time resolution of ≈ 500 ps. The two neutron peaks associated with η production which result from forward and backward scattered neutrons in the TOF spectra were fit and the time difference calculated. The beam momentum relative to the η threshold is determined from this time difference and the lab angle for the neutron.

There is excellent agreement for all momenta above 700 MeV/ c . Our TOF calibration using K^+ and K^- beams verified that the momentum was indeed the same for both charge states to an accuracy of $\approx \pm 2$ MeV/ c , well within the 1% momentum dispersion of the beam. The proton calibration data below 700 MeV/ c is of poorer quality, so we have extrapolated our calibration below 700 MeV/ c by using the known shape of the momentum dependence on D2 current as determined by the Crystal Ball detector measuring the reaction $\pi^-p \rightarrow \pi^0 n$, subsequent to this experiment. This reaction has been measured for beam momenta as low as 200 MeV/ c and the shape is in good agreement with the proton TOF measurements as well as with an earlier, independent calibration done by another experiment. Based on the variance of the D2 current for the π^+ and π^- beam data, we estimate an uncertainty of 0.5 MeV/ c in the relative mean value for the π^+ and π^- beam momenta. The contribution of this uncertainty to the ratio is small compared to the statistical error and can be ignored.

VI. RELATIVE PION FLUX DETERMINATION

Our primary means of determining the pion flux was the coincidence between the two beam scintillators S1 and ST. The accidental rate was a few percent. Since our measurement involved the ratio of two cross sections, only the relative beam rate for π^+ and π^- needed to be determined. This relative flux ratio was independently monitored via a π - p elastic scattering monitor using the ST counter as a proton target. The π - p elastic monitor consisted of an UP counter located 50° above the beam line as measured from ST and a DOWN counter located symmetrically below the beamline. This angle was chosen because it corresponds to the average laboratory pion scattering angle that equals the proton laboratory recoil angle at these beam momenta. Figure 4 shows a 2-D plot of the UP counter analogue to digital converter (ADC) versus the DOWN counter ADC. An elastically scattered event will appear in one of the two loci in the plot depending on which counter detects the proton with the other counter detecting the pion. By selecting these loci, the elastic events were counted with backgrounds of only a few percent.

To verify the consistency of the beam monitoring, we have plotted in Fig. 5 the ratio of the π^+p and π^-p yields, which is equal to the ratio $d\sigma(\pi^+p \rightarrow \pi^+p)/d\sigma(\pi^-p$

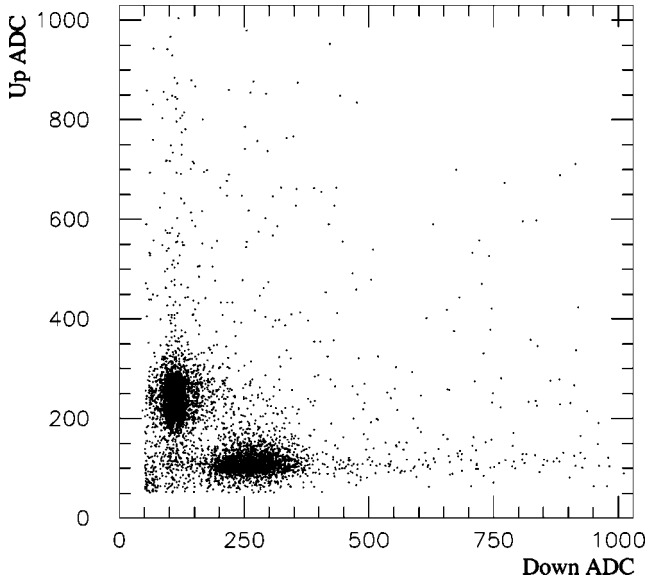


FIG. 4. Scatter plot of the energy deposited in the two beam monitor counters that detected π - p elastic scattering showing the clean identification of pions and protons by pulse height.

$\rightarrow \pi^- p$) at $\theta_{lab} = (50 \pm 2)^\circ$, as a function of beam momentum and compared our results with several partial wave analyses (PWA's) [12,15,16]. The SM95 solutions given for two different scattering angles demonstrate the change in shape of the expected distribution due to the symmetric scattering angle changing from about 51° at 650 MeV/ c to about 49° at 750 MeV/ c . The phase I and II data show excellent agreement with one another as well as reasonable agreement with the PWA's. For comparison, we have also included existing data in this region from Sadler *et al.* [17] and Gordeev *et al.* [18]. There is excellent agreement at 650 MeV/ c and reasonable agreement at 680 MeV/ c . The difference between the two sets could be due to uncertainties in the beam momen-

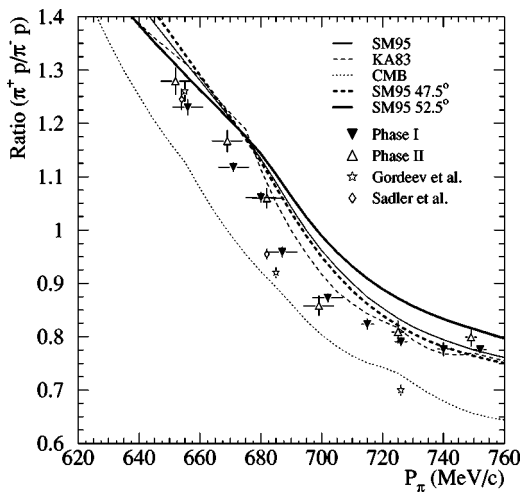


FIG. 5. Ratio of the yields $(\pi^+ p \rightarrow \pi^+ p) / (\pi^- p \rightarrow \pi^- p)$ at $\theta_L \approx 50^\circ$ measured in our experiment along with three different πN partial wave solutions, SM95 [12], KA83 [15], and CMB [16]. The two additional SM95 solutions indicate the variation in the shape of the distribution when the opening angle is varied.

tum which have not been included in the data from Refs. [17,18]. The disagreement between our data and that of Gordeev *et al.* at 725 MeV/ c is due to a disagreement in the $\pi^- p$ elastic data. Our data are consistent with Ref. [18] in the $\pi^+ p$ channel.

The only source of error in the flux monitoring would be due to a difference in the electron and muon contamination in the pion beams. The fraction of electrons in the beam was measured by the Čerenkov counter to be 3–5% depending upon the beam momentum and the percentage was essentially charge symmetric. The muon contamination was determined by range measurement to be $\approx 2\%$ and independent of momentum and polarity in this experiment. Based on $\approx 5\%$ fluctuations in the phase II π^+ flux monitoring relative to phase I, we assign a 10% uncertainty in the determination of the beam contamination of one polarity relative to the other, resulting in a 0.5% systematic uncertainty to the ratio.

VII. CALORIMETER GAIN CALIBRATION

Cosmic ray data were taken continuously throughout the running period to provide a relative gain calibration of the NaI calorimeters. Scintillation counters placed above and below each calorimeter provided the trigger for these events both during and between beam spills. This trigger, along with random triggers for pedestal determination, allowed us to monitor rate-dependent gain shifts in each calorimeter. These shifts were small as expected from the low counting rates. The energy deposited by the cosmic rays does not provide an absolute calibration. We found that the cosmic ray calibration must be increased by 14% in order to obtain the correct invariant mass for the η . MC simulation of the spectrometer indicated that about 10% of the photon shower energy is not included in the shower reconstruction. The remaining 4% is believed to be due to the combination of several effects: (1) the different way that light is produced in the NaI crystals by photons and cosmic ray muons, and (2) uncertainties in the geometric positioning of the calorimeters relative to the target.

VIII. ETA ANALYSIS

The objective of this experiment was to determine the relative ratio of η production in $\pi^+ d \rightarrow pp \eta$ and $\pi^- d \rightarrow nn \eta$. Each reaction was identified by detecting only the neutral η meson via its two-photon decay mode. The analysis consisted of determining the number of η 's per incident pion for each run. We identified the η meson by reconstructing the two-photon invariant mass from the energy and position of the photon cluster in each spectrometer arm via the relation $M_{12} = \sqrt{2E_1 E_2 (1 - \cos \theta_{12})}$, where the indices 1 and 2 refer to the photons and θ_{12} is their opening angle.

By measuring the ratio of yields, we only have to determine with good precision the relative acceptances, detection efficiencies, and backgrounds for π^+ and π^- . This greatly facilitates the way we determine the η yield from the raw data. We carefully monitored the consistency of the π^+ and π^- data sets as well as the internal agreement of the different runs collected for each data point.

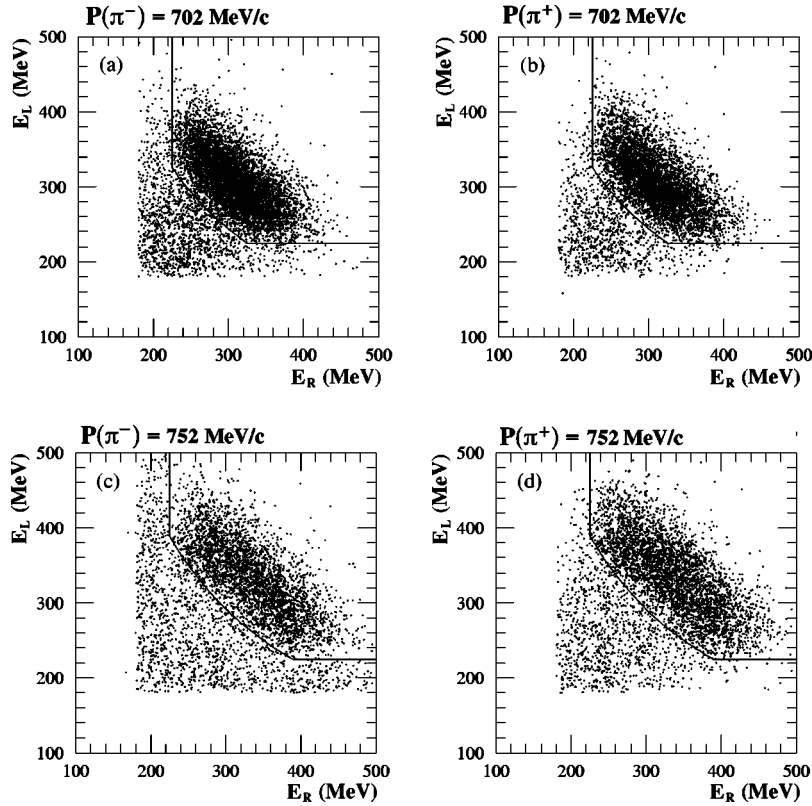


FIG. 6. Four typical examples of the scatter plots of the measured photon energies E_L and E_R of neutral events in the left and right arms of the spectrometer. Plots are phase I data for π^- (left) and π^+ (right) beam polarities for beam momenta of 702 MeV/c (top) and 752 MeV/c (bottom). The solid lines indicate the $E_{L,R}$ cuts used for the data analysis.

In the experiment we recorded all signals that gave a coincidence in the NaI counters, which included neutral and charged events. A neutral event was defined to be one in which none of the veto counters fired. The charged triggers allowed us to determine the fraction of neutral events vetoed by charged particles or photon conversions. Charged events were divided into two categories: single charged events, in which a veto in only one arm fired; and double charged events which required vetoes in both arms to fire. Single charged events were important for verifying that no protons from $\pi^+ d \rightarrow \eta pp$ events hit one of the front vetoes, which would introduce a charge asymmetry in the determination of the ratio. About 3% of the events were rejected because at least one of the vetoes on the upstream sides of the calorimeters fired. This fraction of events was the same for both π^+ and π^- and had no effect on the ratio. The ADC information of all the veto counters was recorded to be used in the offline analysis.

Eta mesons were selected from the neutral events using information provided by the η spectrometer. Figure 6 shows scatter plots of the photon energy deposited in the left spectrometer arm, E_L , versus the energy in the right arm, E_R , for four typical cases. The cutoff of the data below photon energies of 180 MeV is due to a software threshold applied for data reduction. The complete set of scatter plots can be found in Ref. [9]. These plots are useful in establishing our subsequent photon energy cuts to remove background, the main source being $2\pi^0$ production from which two energetic photons are detected in the η spectrometer.

Sample spectra for different $\pi^- p$ reactions at $p_\pi = 750$ MeV/c generated by simulation of the η spectrometer set for a 110° opening angle are shown in Fig. 7. Shown are the two

cluster energies E_R and E_L for η production and different background reactions which generate a neutral trigger. All processes which were simulated for this experiment, including singly- and doubly-charged triggers, are listed in Table I. The $\pi-p$ processes were generated according to the phase space distribution and the $\pi-d$ processes were generated according to the $\pi-p$ phase space with the second nucleon acting as a spectator. The nucleons' internal momentum distribution for the deuteron was included. The spectra of the deuteron reactions are very similar to the $\pi-p$ distributions because the small solid angle acceptance of our detector, not the kinematics, determines the distributions shown.

The event selection consisted of the logical AND of two cuts:

A minimum energy cut, $E_R > E_m$ and $E_L > E_m$. This cut rejects any event for which the energy in either arm is less than the minimum value E_m . The value of E_m varied between 200 and 225 MeV depending on the opening angle of the spectrometer.

A hyperbolic cut, $E_R E_L > E_c^2$. This cut is particularly useful to suppress the $2\pi^0$ background discussed below. The value of E_c was calculated using the relation $E_c^2 = 0.25(E_p - f\sigma_p)^2$, where E_p is the peak value of the measured η energy distribution at each opening angle for each pion momentum, σ_p is the width of the η -energy distribution, and f is a numerical factor ranging from 1.9 to 2.3 being determined from MC studies to minimize the $2\pi^0$ background without losing η mesons.

The region selected by these cuts is indicated in Fig. 6 by the solid lines. The total η energy, E_η , is the sum of the photon energies deposited in the two spectrometer arms,

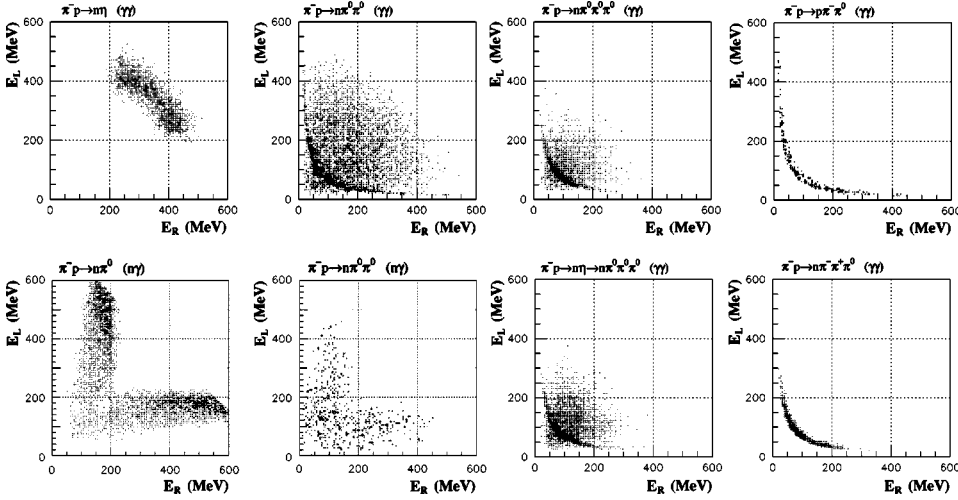


FIG. 7. Scatter plots of the simulated photon energies E_L and E_R at a spectrometer opening angle of 110° for $P_\pi=750$ MeV/c. The top left figure is for the $\eta \rightarrow \gamma\gamma$ reaction. The remaining plots show various background reactions. The detected particles for each reaction are specified in parentheses.

$E_\eta = E_L + E_R$. Table II lists the central value E_p and the measured width σ_E of the E_η distribution in our experiment for all beam momenta and spectrometer opening angles of both phase I and II. Also listed are the difference $\Delta E_{p\pm}$ in the peak E_η value for the π^+ and corresponding π^- data, the difference $\Delta\sigma_{E\pm}$ in the widths, and the difference $\Delta E_{c\pm}^2$ in the cut energy. This table shows the complete equality of the π^+ and π^- data at each beam momentum. It demonstrates that our analysis is fully ‘‘charge symmetric.’’

We have calculated the invariant mass of the neutral events both with and without the photon-energy cuts. The

TABLE I. List of simulated reactions at $P_\pi=750$ MeV/c along with the triggers they could generate. Detection of three neutral particles in the final state can safely be ignored since this has an extremely small probability.

Channel	Neutral	Single charge	Double charge
$\pi^- p \rightarrow \pi^- p$			$\pi^- p$
$\pi^- p \rightarrow \pi^+ \pi^- n$		$\pi^+ n$	$\pi^+ \pi^-$
$\pi^- p \rightarrow \pi^- \pi^0 p$	$\pi^0 \rightarrow \gamma\gamma$	$\gamma p, \gamma\pi^\pm$	$\pi^- p$
$\pi^- p \rightarrow \pi^+ \pi^- \pi^0 n$	$\gamma\gamma(\pi^0)$	$\gamma n, \gamma\pi^\pm$	$\pi^+ \pi^-$
$\pi^- p \rightarrow \pi^0 n$	$\gamma\gamma(\pi^0), \gamma n$		
$\pi^- p \rightarrow \eta n$	$\gamma\gamma(\pi^0)$		
$\pi^- p \rightarrow 2\pi^0 n$	$\gamma\gamma, \gamma n$		
$\pi^- p \rightarrow 3\pi^0 n$	$\gamma\gamma, \gamma n$		
$\pi^- d \rightarrow \pi^- d$			$\pi^- d$
$\pi^+ d \rightarrow \pi^+ d$			$\pi^+ d$
$\pi^- d \rightarrow \pi^- p n$		$\pi^- n, p n$	$\pi^- p$
$\pi^+ d \rightarrow \pi^+ p n$		$\pi^+ n, p n$	$\pi^+ p$
$\pi^- d \rightarrow n n$	$n n$		
$\pi^+ d \rightarrow p p$			$p p$
$\pi^- d \rightarrow \pi^0 n n$	$\gamma\gamma(\pi^0), \gamma n, n n$		
$\pi^+ d \rightarrow \pi^0 p p$	$\gamma\gamma(\pi^0),$	γp	$p p$
$\pi^- d \rightarrow \eta n n$	$\gamma\gamma(\eta), \gamma n, n n$		
$\pi^+ d \rightarrow \eta p p$	$\gamma\gamma(\eta)$	$\gamma p,$	$p p$
$\pi^- d \rightarrow 2\pi^0 n n$	$\gamma\gamma, \gamma n, n n$		
$\pi^+ d \rightarrow 2\pi^0 p p$	$\gamma\gamma$	γp	$p p$

results for four representative cases are shown in Fig. 8. The complete set can be found in Ref. [9]. The data with the energy cuts show a Gaussian peak centered near the η mass. Without the energy cuts, the data show a small secondary peak around 450 MeV due to $2\pi^0$ events. Table III lists the number of η events defined as neutral events with the photon energy cuts as illustrated in Fig. 8 for all data sets obtained in our experiment. Each η peak was fitted by a Gaussian to obtain a central value and width. The deviation of this central value from the known η mass m_η is listed in Table III as Δm ; also given is the width of the invariant mass distribution σ_m . The last two columns in Table III allow the comparison of the π^+ and π^- data by listing the difference in Δm (Δm_\pm) and σ_m ($\Delta\sigma_\pm$) for π^+ and π^- data.

The agreement between the π^+ and π^- data is excellent except at the lowest momentum where the η signal is very small relative to the $2\pi^0$ background discussed below. Note that the width σ_m of the η invariant mass distribution listed in Table III for the phase II data is somewhat larger than under comparable conditions in phase I. This decreased resolution is the result of the different triggering geometry in the photon arms of the η spectrometer used for the two phases. In phase II, we gain acceptance at the expense of energy resolution.

The background is largely from the reaction $\pi^\pm d \rightarrow 2\pi^0 N N$. This background is significant for the lowest pion momenta because the η production cross section is relatively small compared to that from the $2\pi^0$ production. It is also significant at the highest pion momentum where the phase space of the $2\pi^0$ channel begins to encounter the region of the η invariant mass due to the finite resolution of our spectrometer. At the highest momentum of 750 MeV/c, we collected data at four different opening angles to study this background. In phase I we also took data with the spectrometer arms extended to 87.5 cm from the target. These data have reduced $2\pi^0$ background as a result of the smaller range of opening angles accepted by the detector and the improved angular resolution. These data are listed in Tables II and III with the opening angle marked as ‘‘110^{ext}.’’

All other backgrounds can be easily separated from η production by the cuts shown in Fig. 6. Figure 8 shows the

TABLE II. Properties of E_η in phase I and phase II. E_p and σ_E are the position and width of the η energy peak. $\Delta E_{p\pm}$, $\Delta\sigma_{E\pm}$, and $\Delta E_{c\pm}^2$ are the differences between the π^+ and π^- data of the peak positions, widths, and the values for the hyperbolic cut, respectively.

p_π (MeV/c)	θ_{open}^{spec} (Deg.)	π^+d		π^-d		$\Delta E_{p\pm}$ (MeV)	$\Delta\sigma_{E\pm}$ (MeV)	$\Delta E_{c\pm}^2$ ($\times 10^3$) (MeV ²)
		E_p (MeV)	σ_E (MeV)	E_p (MeV)	σ_E (MeV)			
Phase I								
656	150	584.8	31.7	582.9	33.7	1.9 ± 3.2	-2.1 ± 2.8	1.6 ± 3.4
671	140	595.6	32.4	595.9	34.1	-0.3 ± 1.2	-1.7 ± 0.9	0.8 ± 1.2
680	140	598.9	33.5	598.5	33.3	0.4 ± 1.3	0.1 ± 1.1	0.0 ± 1.4
687	130	611.2	33.2	611.6	34.8	-0.3 ± 1.1	-1.6 ± 0.9	0.8 ± 1.1
702	130	612.8	35.4	613.8	36.6	-0.9 ± 0.8	-1.2 ± 0.8	0.4 ± 0.9
715	120	640.7	33.5	638.6	34.2	2.1 ± 1.1	-0.6 ± 1.0	1.0 ± 1.4
726	120	640.0	38.3	639.8	38.0	0.2 ± 1.1	0.3 ± 1.0	-0.1 ± 1.3
740	110	661.8	34.9	668.3	36.2	-6.5 ± 1.3	-1.3 ± 1.2	-1.2 ± 1.6
752	130	609.6	45.1	610.7	42.2	-1.2 ± 4.2	2.9 ± 3.6	-1.7 ± 4.2
752	110	667.5	37.5	670.7	39.8	-3.3 ± 1.3	-2.3 ± 1.1	0.4 ± 1.5
752	100	673.0	37.6	671.8	38.6	1.2 ± 1.8	-1.0 ± 1.4	1.0 ± 2.0
752	110 ^{ext}	664.2	36.9	667.2	35.1	-3.0 ± 2.7	1.9 ± 2.4	-2.0 ± 3.3
Phase II								
652	150	591.8	34.4	593.6	34.3	-1.8 ± 3.1	0.0 ± 2.2	-0.5 ± 2.7
669	140	606.2	34.6	605.3	37.1	0.9 ± 1.4	-2.5 ± 1.4	1.6 ± 1.7
682	130	618.2	36.0	618.3	36.7	-0.1 ± 1.2	-0.7 ± 1.0	0.4 ± 1.3
699	130	624.5	38.7	625.3	36.7	-0.8 ± 0.9	2.0 ± 1.0	-1.4 ± 1.2
725	120	647.0	39.6	647.8	41.0	-0.9 ± 1.5	-1.4 ± 1.2	0.6 ± 1.8
749	120	650.7	46.6	654.2	49.5	-3.5 ± 2.0	-2.9 ± 1.7	0.6 ± 2.1
749	110	669.4	41.7	671.7	43.2	-2.3 ± 2.0	-1.6 ± 1.4	0.2 ± 2.0

two-neutral-cluster invariant mass spectra with and without the 2γ energy selection defined by the cuts shown in Fig. 6. The minimum energy cuts represented by the vertical and horizontal lines effectively eliminated a significant background which came from two-cluster events in which one was very low energy and the other very high. The simulation plots of Fig. 7 indicate these events predominantly come from the detection of a neutron and one photon from the π^0n and $2\pi^0n$ channels. These events extend underneath the η peak in the invariant mass spectrum; but they can be easily removed with cuts on the cluster energies.

The hyperbolic cut was applied primarily to define the η events which determine the yield. Its value was set to a value two standard deviations below the central value of the η peak in the plot of the total energy of the two photons.

These cuts do not completely eliminate the $2\pi^0$ background in the η region. This remaining background was studied by plotting the total energy from the two photons rather than the invariant mass since the $2\pi^0$ background is nearly linear in this variable near the η region. A slice of constant width along the line where $E_L = E_R$ in the E_L vs E_R plot with no cuts was used to study the background. This insured that the integrated background could be extrapolated into the η region.

The variation of the experimental resolution for the different experimental conditions made it difficult to perform a consistent background subtraction from the η yields. Instead,

the amount of possible background under the η peak was estimated assuming two possible endpoints for the background distribution: (1) the maximum background energy occurs at the 2σ value above the mean η energy, and (2) the endpoint coincides with the mean value. The former is an extreme condition and the latter is a reasonable assumption according to the simulation of the $2\pi^0$ reaction. A linear fit to the background distribution allowed an extrapolation of this background underneath the peak so that an estimate of the maximum possible background could be made for both cases. The results indicated that the backgrounds were all less than 10% for case (1) and less than 5% for case (2) except at the very lowest momentum and at the very highest when the opening angle was 130° . In these cases the background was $\approx 20\%$ and 10% , respectively. More importantly, however, the fractional backgrounds for π^+ and π^- were the same within the statistical precision of the data with deviations $\approx 0.3\%$. This means that the percent change in the yield is the same for both π^+ and π^- and so no background subtraction was done since the effect of this subtraction would cancel in the calculation of the ratio. Only the 750 MeV/c data at 130° showed an asymmetry which exceeded the statistical precision and required a correction of 8% to the value of the ratio.

The cancellation of background in the ratio was confirmed in the 750 MeV/c data where we had ratios for 3 different opening angles corresponding to significantly different back-

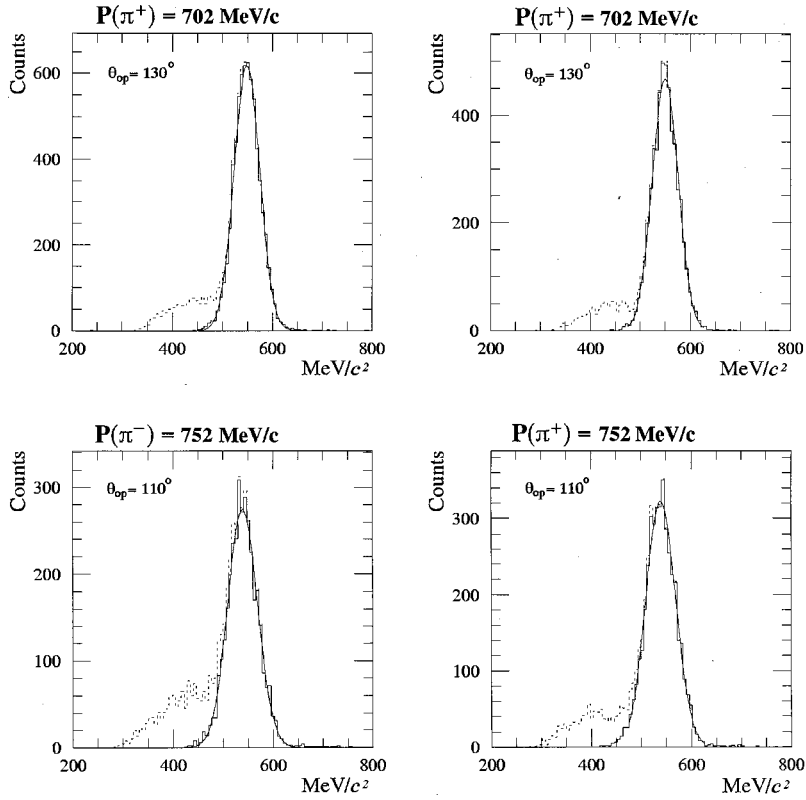


FIG. 8. Typical 2γ invariant mass spectra for two representative beam momenta. The background is largely due to the reaction $\pi^\pm d \rightarrow 2\pi^0 NN$. Solid histogram corresponds to data with E_L - E_R cuts applied. Dotted histogram is without the E_L - E_R cuts. Solid curve is a Gaussian fit to the data.

ground contributions. The results of the ratios for these three sets of data were statistically consistent with one another. We have allowed for an uncertainty in the ratio due to this unsubtracted background by adding a 1% uncertainty in quadrature with the final error of the calculated ratios for all momenta except 655 and 670 MeV/c where we have added 2% and the 750 (130°) data where we have added 4%.

IX. RESULTS

The chief objective of this experiment is to test charge symmetry invariance by means of measuring the ratio $R \equiv d\sigma(\pi^+ d \rightarrow pp\eta)/d\sigma(\pi^- d \rightarrow nn\eta)$. When CS is valid R_c must be unity where R_c is the value of R after the corrections for the n - p mass difference and the Coulomb interactions have been made.

The ratio R is identical to R_{exp} , the ratio of the η yields, $R_{exp} \equiv (\eta \text{ yield in } \pi^+ d)/(\eta \text{ yield in } \pi^- d)$ when the following conditions are valid: (a) the π^+ and π^- beams have the same phase space, (b) the η yields are extracted in the same manner for π^+ and π^- , (c) the veto counters do not affect the ratio of η yields, and (d) the neutron interactions in the NaI calorimeter do not lead to false η events or cause a loss of good η events in the π^- data. We have made various tests to show that R_{exp} is not affected outside the quoted errors by the η selection criteria, the $2\pi^0$ background under the η peak, the π^+ and π^- beam parameters, and the neutron interactions in the NaI. Details of this analysis are given in Ref. [9]. We have analyzed the single and double charged event samples and found they do not affect R_{exp} either. We

conclude that our measured value for R_{exp} is equal to the value for R .

Table IV presents the experimental results for R . The error quoted for R includes the statistical error and the background correction uncertainty. It does not include the absolute uncertainty in the beam momentum nor the relative uncertainty in the beam normalization. The ratios show good agreement between phase I and II data sets. Also listed in this table are the incident beam momenta p_π , the uncertainty in the beam momentum, the mean η kinetic energy T_η accepted by our setup, and ΔT_η , the full width at half maximum of T_η . The last two columns are the result of correcting the ratio for threshold effects discussed below.

Figure 9 compares our results with the predictions of the theoretical model of Sec. II. The figure is divided into five vertical slices, each one corresponding to a different opening angle of the η spectrometer. The theoretical curves have been evaluated for the different experimental opening angles resulting in the apparent discontinuities of the distributions. The theoretical curves represent different values of the π - η mixing angle $\theta_{\pi\eta}$ of 0°, 1°, 2°, 3°, and 4°. The best agreement between our results and the model is for $\theta_{\pi\eta} = (1.5 \pm 0.4)^\circ$ obtained by minimizing the χ^2 value. Systematic errors in the model have not been included in this value. We have included in this error estimate a contribution of 0.3° from the uncertainty in the absolute value of the beam momentum. Figure 10 shows the η production as a function of its c.m. scattering angle $\cos(\theta_\eta)$ normalized to theoretical differential cross section distributions for two beam momenta of 670 MeV/c and 746 MeV/c with spectrometer

TABLE III. Properties of the η invariant mass peak in phase I and phase II. θ_{open}^{spec} is the spectrometer opening angle corresponding to the nominal opening angle between the two photons from $\eta \rightarrow \gamma\gamma$. N_η is the number of η 's obtained; Δm is the deviation of the experimental centroid value of the peak from the known value of the η invariant mass. σ_m is the Gaussian width of the peak and Δm_\pm and $\Delta\sigma_\pm$ are the differences in the values of Δm and σ_m between the π^+d and π^-d channels.

P_π (MeV/c)	θ_{open}^{spec} (Deg.)	π^+d			π^-d			Δm_\pm (MeV)	$\Delta\sigma_\pm$ (MeV)
		N_η	Δm (MeV)	σ_m (MeV)	N_η	Δm (MeV)	σ_m (MeV)		
Phase I									
656	150	436	14.1	23.7	547	7.9	25.8	6.2 ± 1.7	-2.1 ± 1.5
671	140	2418	5.7	25.7	3085	7.2	25.1	-1.5 ± 0.7	0.7 ± 0.6
680	140	2254	9.0	25.4	3548	8.2	24.6	0.8 ± 0.7	0.8 ± 0.5
687	130	2934	3.3	25.8	3828	3.3	25.8	0.0 ± 0.6	0.1 ± 0.5
702	130	6728	1.6	25.8	5107	2.2	26.0	-0.6 ± 0.5	-0.2 ± 0.4
715	120	3562	1.2	26.5	3378	-1.2	25.9	2.5 ± 0.6	0.7 ± 0.5
726	120	6274	-3.3	27.8	6753	-4.6	27.2	1.3 ± 0.5	0.6 ± 0.4
740	110	2751	-6.0	30.2	2644	-4.7	28.6	-1.3 ± 0.8	1.6 ± 0.6
752	130	1279	0.3	29.0	1457	0.2	28.8	0.1 ± 1.2	0.3 ± 0.9
752	110	3492	-8.1	29.8	4068	-8.3	29.9	0.1 ± 0.7	-0.1 ± 0.5
752	100	2224	-13.2	31.3	1672	-15.2	30.1	2.0 ± 1.0	1.2 ± 0.9
752	110 ^{ext}	789	-12.5	30.4	802	-13.0	28.5	0.5 ± 1.5	1.9 ± 1.3
Phase II									
652	150	778	7.6	31.1	858	12.6	29.6	-4.9 ± 1.6	1.4 ± 1.4
669	140	2167	6.6	30.1	2228	8.8	30.4	-2.3 ± 1.0	-0.2 ± 0.8
682	130	3390	6.4	29.2	4048	6.2	30.1	0.2 ± 0.7	-1.0 ± 0.6
699	130	4777	7.2	30.4	3816	6.4	29.7	0.8 ± 0.7	0.7 ± 0.5
725	120	3953	-0.8	30.9	3880	1.3	32.1	-2.1 ± 0.7	-1.2 ± 0.6
749	120	3815	-5.9	33.9	3643	-2.5	33.2	-3.4 ± 0.9	0.7 ± 0.7
749	110	3620	-5.9	32.8	4000	-3.8	31.5	-2.0 ± 0.8	1.4 ± 0.6

opening angles of 140° and 130° , respectively. The dashed lines represent predictions without beam momentum dispersion; the thick lines include a momentum dispersion of 1%. It is apparent from these figures that our model describes the dependence of R on the beam momentum and η spectrometer opening angle very well.

We have not compared the absolute η yield with theory since neither experiment nor theory were designed to determine absolute cross sections. The systematic uncertainty in the determination of the absolute cross section is principally due to the acceptance and this effect cancels completely in the ratio of yields. We have ascertained that uncertainties in the model which could cause a 50% change in the π^+ and π^- total cross sections only change the ratio by $<0.5\%$. Similarly, the uncertainty in the hadronic part of our model has an ignorably small effect on the ratio. In our model most of the hadronic interactions that affect the charge symmetry ratio are handled using an effective T -matrix. Thus, several components of the hadronic interactions, such as the final state interaction between the spectator nucleon and the η , are partially accounted for in our model.

One possible improvement of our model would be the inclusion of the Coulomb interaction in the initial state between the pion and deuteron, which has opposite signs for π^+ and π^- . Another would be to improve the Jost function used to account for the nucleon-nucleon interaction so that it

properly describes the reaction when it is not close to threshold.

The value of R listed in Table IV and used in Fig. 9 is not constant with momentum, varying from a value ≈ 1.1 close to threshold to ≈ 0.9 at the highest beam momentum and largest opening angle. We surmise that the variation of R with beam momentum is largely due to the consequence of the n - p mass difference in the final state of η production by π^+ as compared to π^- . We have investigated this by converting R_{exp} into R_{cal} where the latter is the η production ratio evaluated at identical pion energies above the η production threshold. Since we have made our yield measurements at the same absolute beam momentum this ratio must be calculated by interpolation of the yields measured at the different beam momenta. We have corrected the π^- data for the n - p mass difference and the initial state Coulomb energy difference of 0.8 MeV. This correction is done in the center of mass so that the beam pion energy E_π^{cm} is the same for π^+ and π^- . The results for R_{cal} are listed in Table IV and are shown in Fig. 11. The ratio at the lowest energy is most uncertain because of the proximity to threshold. The results are consistent within errors with a constant asymmetry as a function of energy above threshold and yield a mean value $\bar{R}_{cal} = 0.938 \pm 0.008$. The dashed lines mark the one standard deviation limits for this result. We estimate the systematic

TABLE IV. Ratio (R) of η yields from π^+d and π^-d reactions for phase I and phase II. The uncertainty for the ratio R consists of the statistical and background correction uncertainties; it does not include the uncertainty in the absolute value of the beam momentum. T_η is the mean accepted η kinetic energy and ΔT_η is the full width half maximum of the accepted distribution. R_{cal} is R corrected for the different threshold energies which result from differences in the nucleon masses and electromagnetic effects for the two reactions. δE_π^{cm} is the pion's relative c.m. energy above the $pp\eta$ threshold at which the ratio was calculated.

p_π (MeV/c)	θ_{open}^{spec} (Deg.)	T_η (MeV)	ΔT_η (MeV)	$R(\pi^+/\pi^-)$	δE_π^{cm} (MeV)	$R_{cal}(\pi^+/\pi^-)$
Phase I						
656 ± 5	150	30	37	1.029 ± 0.078	36.0	0.808 ± 0.081
671 ± 5	140	48	51	1.110 ± 0.041	47.2	1.013 ± 0.062
680 ± 5	140	46	45	1.065 ± 0.035	53.9	0.904 ± 0.110
687 ± 5	130	65	54	1.028 ± 0.032	59.1	0.979 ± 0.033
702 ± 5	130	70	65	0.950 ± 0.022	70.2	0.914 ± 0.030
715 ± 2	120	96	63	0.935 ± 0.026	79.7	0.941 ± 0.022
726 ± 2	120	102	76	0.927 ± 0.020	87.8	0.931 ± 0.026
740 ± 2	110	129	63	0.980 ± 0.032	98.0	0.977 ± 0.032
752 ± 2	130	73	67	0.891 ± 0.052	106.8	0.937 ± 0.056
752 ± 2	110	135	75	0.916 ± 0.026	106.8	0.928 ± 0.030
752 ± 2	100	145	59	0.942 ± 0.037	106.8	0.957 ± 0.037
752 ± 2	110^{ext}			0.892 ± 0.051	106.8	0.902 ± 0.062
Phase II						
652 ± 5	150	29	37	1.109 ± 0.058	33.0	0.891 ± 0.066
669 ± 5	140	47	51	1.077 ± 0.043	48.4	0.910 ± 0.061
682 ± 5	130	64	54	1.034 ± 0.029	58.0	0.951 ± 0.034
699 ± 5	130	68	65	0.978 ± 0.026	67.7	0.945 ± 0.026
725 ± 2	120	101	76	0.918 ± 0.025	84.6	0.922 ± 0.025
749 ± 2	120	116	94	0.948 ± 0.028	102.9	0.925 ± 0.031
749 ± 2	110	134	75	0.942 ± 0.028	102.9	0.946 ± 0.033

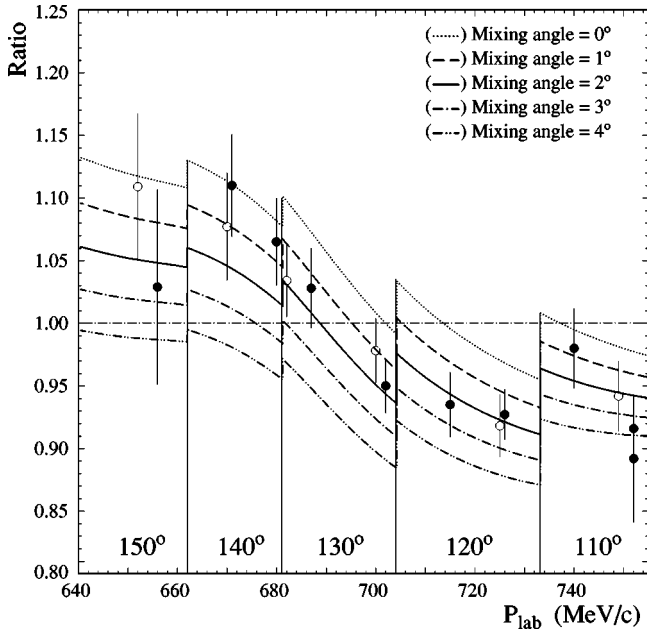


FIG. 9. The final results for $R \equiv d\sigma(\pi^+d \rightarrow pp\eta) / d\sigma(\pi^-d \rightarrow nn\eta)$ calculated from both data sets, phase I (\bullet) and phase II (\circ), compared with the model of Batinić [7] for different values of the π^0 - η mixing angle. Vertical lines separate data taken with the different spectrometer opening angles indicated.

error in R_{cal} to be 0.5% due to the uncertainty in the relative beam momentum, explained in Sec. VI which yields the overall result $\bar{R}_{cal} = 0.938 \pm 0.009$.

X. DISCUSSION AND CONCLUSIONS

Our study of the reactions $\pi^-d \rightarrow nn\eta$ and $\pi^+d \rightarrow pp\eta$ in the incident energy interval just above the η production threshold shows a $(6.2 \pm 0.9)\%$ deviation from charge symmetry in the ratio of the yields of the two processes. There are many factors that influence the cross sections of these two processes and their ratio: the neutron-proton mass difference, EM interactions, initial and final state interactions, off-energy-shell effects, different $NN\eta$ coupling constants, π - η mixing, etc. We have developed a fully relativistic model based on the dominant impulse approximation term which includes π - η mixing and a 1S_0 NN final state interaction in the form of the Jost function. This model does not include off-energy-shell effects, an initial state interaction, nor $NN\eta$ coupling constant effects. A recent study by Garcilazo and Peña [19] investigated the final state interaction and off-energy-shell effects and found them not to be significant. Our model incorporates the details of the experimental setup so the yields, instead of cross sections, could be compared directly.

Comparison of the data with the model shows that the

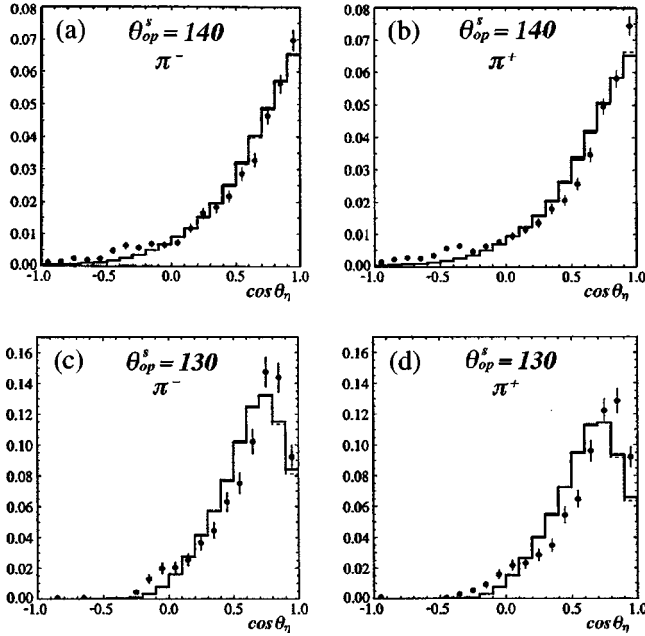


FIG. 10. The angular distributions for η production normalized to our theoretical differential cross sections for 670 MeV/c beam momentum and a spectrometer opening angle of 140° for the reactions $\pi^- d \rightarrow nn \eta$ (a) and $\pi^+ d \rightarrow pp \eta$ (b). (c) and (d) are similar distributions for an opening angle of 130° that compare data at 752 MeV/c with model calculations at 746 MeV/c.

model provides a very good description of the angular distributions and the beam momentum dependence of the ratio. The analysis of the ratio yields a value for the π - η mixing angle $\theta_{\pi\eta} = (1.5 \pm 0.4)^\circ$ which does not include all possible systematic errors from the model, namely, inadequacies in the EM differences in the initial and final states as discussed earlier.

Recent calculations of the mixing angle have been done by Chan *et al.* [20] using QCD sum rules, Maltman and Goldman [21] using a chiral quark model, and Piekarewicz [22] who used an hadronic model. These models included a possible q^2 dependence in the mixing angle. They yield values of $\theta_{\pi\eta} = (0.75 - 0.83)^\circ$. It is not clear whether the octet-singlet mixing is properly included. Leutwyler [23] argues that the effect of the octet-singlet mixing is to increase the mixing angle by about 20% which would yield values no greater than 1° . Using a method of saturating anomalous Ward identities with π^0 , η , and η' mesons which naturally includes octet-singlet mixing, Bagchi [24] has calculated a value of $\theta_{\pi\eta} = (1.95 \pm 0.75)^\circ$; twice the size of values given above. He also obtains a value for the octet-singlet mixing of -20° consistent with other more recent calculations of this angle. The factor of two difference between Bagchi and the others could be due to the way the octet-singlet mixing is handled [23]. Our result falls between these two different values of the mixing angle and the size of our uncertainty

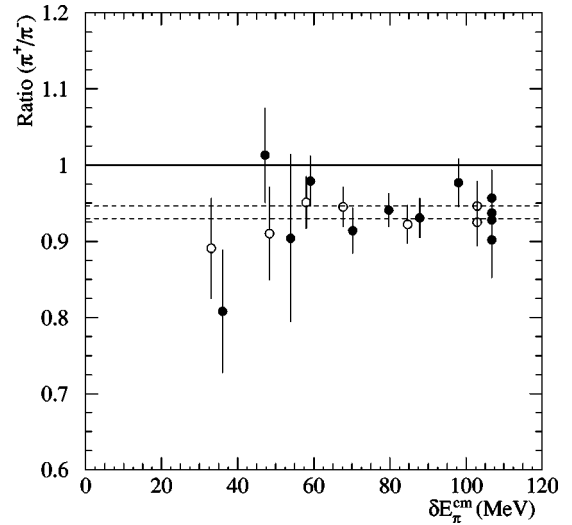


FIG. 11. Comparison of the ratio $R \equiv d\sigma(\pi^+ d \rightarrow pp \eta) / d\sigma(\pi^- d \rightarrow nn \eta)$ for phase I (\bullet) and phase II (\circ) after adjustment for the n - p mass difference and initial state Coulomb interaction. The dashed lines indicate the one- σ band for the mean asymmetry determined from the data. δE_π^{cm} is the relative c.m. energy of the pion above the $pp \eta$ threshold.

prevents us from excluding either. The fact that our result is significantly larger than the $\approx 1^\circ$ calculations could be due to the octet-singlet mixing and/or nuclear medium effects.

Clearly, improvement of this technique by the use of a large acceptance detector to provide a better determination of the angular dependence as well as higher statistics combined with a more refined η production model could significantly reduce the uncertainty in the determination of the mixing angle. Another advantage of this method is the potential exploration of the mixing angle as a function of q^2 of which there is much theoretical disagreement. This is important for understanding CSB since the π - η mixing contribution must be determined by extrapolation. Our study is the first determination of the π - η mixing angle from a nuclear reaction process.

ACKNOWLEDGMENTS

We thank the AGS staff for their assistance with the implementation of this work and specifically the cryogenic target group for their effort in providing the liquid deuterium target. We specifically want to thank S. Philips, A. Shafi, H. Avazian, and L. Alfieri from George Washington University and J. Caire and B. Draper from Abilene Christian University for their assistance with the experimental installation. This experiment was supported in part by the U.S. DOE and NSF, the Russian Ministry of Science and Technology, the Russian Foundation of Basic Research, and the Russian State Scientific-Technical Program: Fundamental Nuclear Physics.

- [1] G. A. Miller, B. M. K. Nefkens, and I. Šlaus, *Phys. Rep.* **194**, 1 (1990).
- [2] S. L. Kramer *et al.*, *Phys. Rev. Lett.* **33**, 505 (1974).
- [3] A. B. Wicklund *et al.*, *Phys. Rev. D* **17**, 1197 (1978).
- [4] Particle Data Group, C. Caso *et al.*, *Eur. Phys. J. C* **3**, 1 (1998), see p. 110.
- [5] J. Gasser and H. Leutwyler, *Phys. Rep.* **87**, 77 (1982).
- [6] F. Wang, L. Deng, and G. Wu, *Nucl. Phys.* **A537**, 327 (1992).
- [7] M. Batinić *et al.*, in *Proceedings of the 15th International Conference on Few-Body Problems in Physics, 1997*, edited by L. P. Kok, J. C. Bacelar, and A. E. L. Dieperink (Groningen, The Netherlands, 1997), Book of Contributions, p. 419.
- [8] M. Batinić, I. Šlaus, A. Švarc, and B. M. K. Nefkens, *Phys. Rev. C* **51**, 2310 (1995); *Few-Body Syst., Suppl.* **9**, 219 (1995); *Phys. Rev. C* **57**, 1004 (1998); M. Batinić, I. Dadić, I. Šlaus, A. Švarc, B. M. K. Nefkens, and T. S. H. Lee, *Phys. Scr.* **58**, 15 (1998).
- [9] A. Marušić, Ph.D. dissertation, University of Zagreb, 1996.
- [10] M. P. Locher and A. Švarc, *Z. Phys. A* **338**, 89 (1991); *Fizika (Zagreb)* **22**, 549 (1990).
- [11] I. Šlaus, in *Proceedings of the Seventh Conference on Mesons and Light Nuclei '98, Prague-Práhonice, Czech Republic, 1998*, edited by J. Adam, P. Bydžovský, J. Dobeš, R. Mach, J. Mareš, and M. Sotona (World Scientific, Singapore, 1999).
- [12] R. A. Arndt *et al.*, Solution obtained from the SAID program available from http://said.phys.vt.edu/said_branch.html
- [13] J. C. Peng, in *Proceedings of The Third International Symposium of Pion-Nucleon and Nucleon-Nucleon Physics, Gatchina, USSR, 1989*, edited by S. Kruglov and I. Lopatin (Academy of Sciences, USSR, Leningrad, 1989), pp. 315–329; M. J. Leitch *et al.*, *Nucl. Instrum. Methods Phys. Res. A* **374**, 299 (1996).
- [14] The GEANT3 program is described in the web version of CERN long writeup W5013 which can be found at <http://wwwinfo.cern.ch/asd/index.html>
- [15] G. Höhler, in *Pion-Nucleon Scattering*, edited by H. Schopper, Landolt-Börnstein (Springer, New York, 1983), Vol. 9, Part b.
- [16] R. E. Cutkosky *et al.*, *Phys. Rev. D* **20**, 2804 (1979); **20**, 2839 (1979).
- [17] M. E. Sadler *et al.*, *Phys. Rev. D* **35**, 2718 (1987).
- [18] V. A. Gordeev *et al.*, *Nucl. Phys.* **A364**, 408 (1981).
- [19] H. Garcilazo and M. T. Peña, *Phys. Rev. C* **59**, 2389 (1999).
- [20] Chuan-Tsung Chan, E. M. Henley, and T. Meissner, *Phys. Lett. B* **343**, 7 (1995).
- [21] Kim Maltman and T. Goldman, Los Alamos Report LA-UR-92-2910, 1992.
- [22] J. Piekarewicz, *Phys. Rev. C* **48**, 1555 (1993).
- [23] H. Leutwyler, *Phys. Lett. B* **374**, 181 (1996).
- [24] B. Bagchi, *Phys. Rev. D* **41**, 2871 (1990).